Analysis of MMC Energy-based Control Structures for VSC-HVDC Links

Enric Sánchez-Sánchez, *Student Member, IEEE,* Eduardo Prieto-Araujo, *Member, IEEE,* Adrià Junyent-Ferré, *Member, IEEE,* and Oriol Gomis-Bellmunt, *Senior Member, IEEE*

Abstract

An analysis of control structures for Modular Multilevel Converters (MMC) used in High-Voltage Direct Current (HVDC) applications is addressed. In particular, the study focuses on the case of a point-to-point link with master-slave control, considering an energy-based scheme (also known as closed-loop or energy-controlled) for the MMC, meaning that the internal energy of the converter is explicitly controlled. With such an approach, the MMC internal energy can be controlled independently from the energy of the HVDC link, and whereas the internal capacitance of the MMC depends on the converter's rating, the capacitance at the DC terminal depends on the cable length. Therefore, several possibilities regarding the outer control structure (internal energy and DC voltage) arise, affecting the overall dynamics differently. Whereas for a long link the classic control structures should perform well, for shorter links the transient performance might not be acceptable and other alternatives shall be used instead. Different control structures are presented and evaluated in this paper through small-signal and frequency-domain analysis, and validated through time-domain simulation with Matlab® Simscape Power Systems™.

Index Terms

MMC, HVDC transmission, master-slave, control structure, energy-based control.

I. Introduction

High Voltage DC (HVDC) is becoming a relevant technology within the power system. Submarine connections for offshore wind farms and very large distances are its main applications [1]. Line-Commutated Converter (LCC) is already a well-established and mature technology for HVDC. However, it presents some disadvantages, such as the necessity of polarity change to enable power flow reversal, the requirement of an AC grid for feasible operation and

Manuscript received September 15, 2017; revised December 15, 2017; accepted January 18, 2018. Date of publication March XX, 2018, date of current version March XX, 2018. This work has been funded in part by the Spanish Ministry of Economy and Competitiveness under Project ENE2015-67048-C4-1-R. This research was co-financed by the European Regional Development Fund (ERDF).

Enric Sánchez-Sánchez, Eduardo Prieto-Araujo and Oriol Gomis-Bellmunt are with the Electrical Engineering Department, Centre d'Innovació Tecnològica en Convertidors Estàtics i Accionaments (CITCEA-UPC), Universitat Politècnica de Catalunya, ETS d'Enginyeria Industrial de Barcelona, Barcelona 08028, Spain (e-mails: {enric.sanchez.sanchez,eduardo.prieto-araujo,gomis}@citcea.upc.edu).

Adrià Junyent-Ferré is with the Department of Electrical and Electronic Engineering, South Kensington Campus, Imperial College London, London SW7 2AZ, United Kingdom (e-mail: adria.junyent-ferre@imperial.ac.uk).

Color versions of one or more of the figures in this paper are available online at http://ieeexplore.ieee.org.

Digital Object Identifier XXXXXXX

the necessity of bulky filters. Thus, the Voltage Source Converter (VSC) based technology arises as an alternative, yielding bidirectional capability, independent active and reactive power control and space reduction [2]. More specifically, the Modular Multilevel Converter (MMC) has emerged as the preferred VSC alternative because of low losses, low harmonic distortion, scalability and redundancy [3], [4]. However, the control of MMC becomes more challenging than the classic two-level (2L) VSC, due to the extra degrees of freedom inherent to its topology. The different control schemes available in the literature can be classified as follows. First, the non-energy-controlled approach, also known as uncompensated modulation [5], such as direct voltage modulation [6] or open-loop modulation [7]. These are known to be asymptotically stable but their transients depend on the converter impedances rather than being imposed by a controller, which can lead to slow time constants or undesirable overshoots, specially in faulty scenarios [8]. Furthermore, they cause disturbances that lead to circulating currents. However, they are typically eliminated including the so-called Circulating Current Suppressing Control (CCSC) [9]. Second, the energy-controlled approach, also known as compensated modulation [5] or closed-loop [10]. In this case, parasitic voltage components do not appear, but arm-energy controllers are needed to ensure an asymptotically stable system [11].

Linear models are useful for small-signal analysis (stability, eigenvalues, participation factors) [5], [12], [13] and for control design assessment by means of linear tools [14], [15]. Several efforts have been made regarding the linear modeling of the MMC, for both energy-controlled and non-energy-controlled approaches. A steady-state time-invariant (SSTI) model is required to enable linearization. In this paper, an energy-controlled scheme is considered, as it presents the advantage of controlling the internal energy of the MMC, which improves the performance and the stability, avoiding poorly damped oscillation modes introduced by the CCSC in the non-energy-controlled approach [16]. However, there are some issues with respect to the existing literature in this field. Usually, only small step changes are performed in order to validate the linear model with a benchmark non-linear model, ignoring the transient performance in worse scenarios. Moreover, the size of the capacitor introduced in the DC terminals is usually representative of relatively long cables, avoiding the case of short HVDC links. Some examples are summarized next.

In [17], a small-signal model of an MMC with droop DC voltage control and total energy control is derived. A relatively big capacitor is included in the DC terminals, which may improve the DC dynamics and is not a proper approach for the case of a short HVDC link. Also, no strict constraints are considered for the transient performance. In [18], a comparison between two-level and MMC approaches for an HVDC link is presented, showing a significant difference regarding the DC capacitance. However, the length of the cable is unknown and the performance is not the matter of study of the mentioned paper. In [19], the output of the DC voltage controller is used as a reference for the zero-sequence circulating current, whereas the output of the total energy controller is used as a reference for the grid active current, thus inverting the classic control structure and yielding a more consistent transient performance. However, no insight is given for the case of smaller capacitances and for higher transient requirements.

The contribution of this paper is to evaluate different control structures for the outer loops of the master converter in an MMC-based HVDC link. Small-signal analysis and frequency-domain tools are used in order to evaluate the performance in the whole frequency range, complementing the time-domain analysis. The effect of the capacitance in the DC side is emphasized, yielding worse results as its value decreases, which corresponds to shorter links.

Section II presents a description of the system under study. In Section III, the mathematical model of such system and the MMC control are developed. The overall linearized system is presented in Section IV. Different control structures are presented in Section V, which are evaluated in Section VI, analyzing them and raising their issues. Finally, conclusions are drawn in Section VII.

II. System description

The system under study (Fig. 1) consists of an MMC-HVDC symmetrical monopole link. In such configuration, a master-slave control is a typical approach, meaning that one converter regulates the DC voltage whereas the other controls the active power through the link. Also, reactive power can be controlled in both AC side terminals independently.

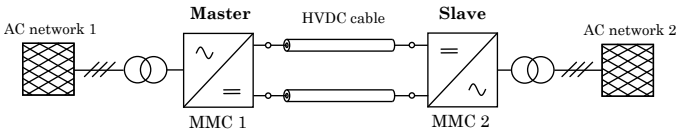

Fig. 1. Point-to-point HVDC link

The MMC structure is presented in Fig. 2. It consists of six arms, each of them including N_{arm} half-bridge submodules with a capacitance C_{SM}, and an arm reactor in series. Submodules are controlled individually, either inserting or bypassing the capacitor. The three legs correspond to the three phases (a, b and c) each of them containing two arms. The six arms synthesize the required voltages in order to achieve the desired power exchange between the AC and the DC side and to handle the internal energy balance of the converter.

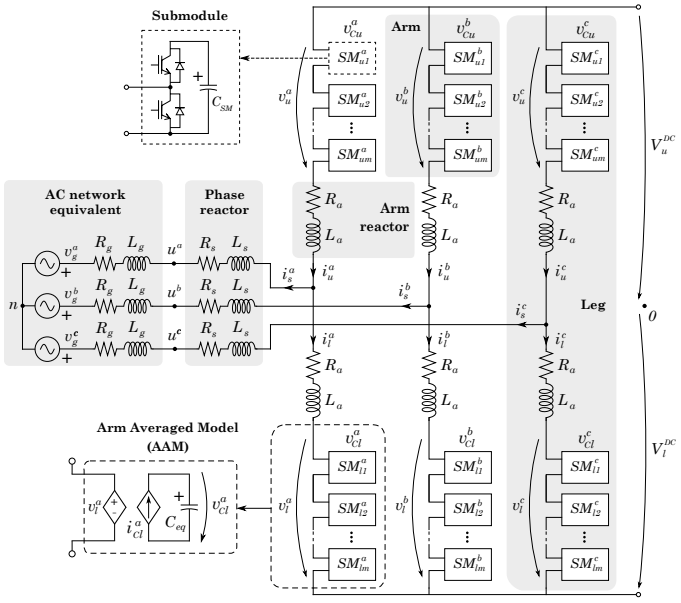

Fig. 2. Electrical model of the MMC connected to a grid Thévenin equivalent

The control scheme used (closed-loop approach) is presented in Fig. 3. Two main parts can be distinguished:

- In the top side, the DC voltage control (master) or the AC active power control (slave) together with the reactive power setpoint yield the grid side current references for the grid side current loop.
- In the bottom side, the total energy and the energy balancing controls yield the circulating current references for the circulating current loop.

Also, a Phase Locked Loop (PLL) tracks the AC voltage in the point of connection with the AC grid. With both current loops outputs, the six arm voltages can be calculated. Finally, the modulation and the cells balancing algorithms are responsible of generating such voltages through an adequate commutation of the submodule switches [20].

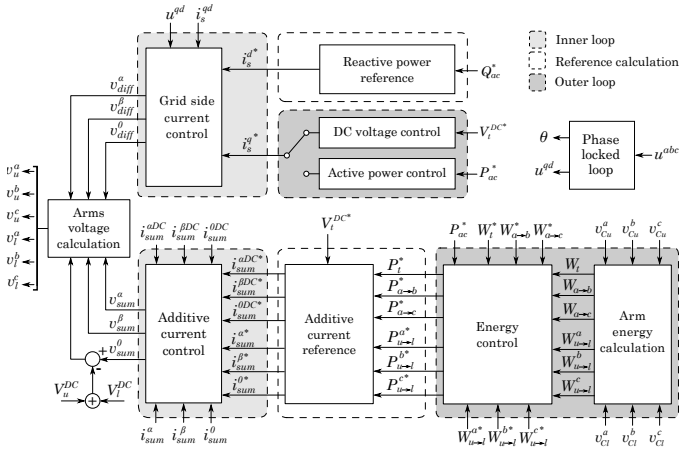

Fig. 3. MMC overall control system

III. System modeling

A. MMC connected to grid electrical circuit

The electrical circuit equations per phase ($j = a, b, c$) are

$$V_u^{DC} - v_u^j - v_g^j - v_n = R_a i_u^j + L_a \frac{di_u^j}{dt} + (R_s + R_g) i_s^j + (L_s + L_g) \frac{di_s^j}{dt} \quad (1)$$

$$-V_l^{DC} + v_l^j - v_g^j - v_n = -R_a i_l^j - L_a \frac{di_l^j}{dt} + (R_s + R_g) i_s^j + (L_s + L_g) \frac{di_s^j}{dt} \quad (2)$$

being

R_a, L_a: arm resistance and inductance.

R_s, L_s: AC grid filter resistance and inductance.

V_u^{DC}, V_l^{DC}: upper and lower voltages of the HVDC link.

v_g^j: Thévenin AC grid voltage.

v_u^j, v_l^j: voltages applied by the upper and lower arms.

i_u^j, i_l^j: current flowing through the upper and lower arms.

i_s^j: AC grid current.

For convenience, the following variable change is defined

$$\begin{cases} v_{diff}^j \triangleq \dfrac{1}{2}(-v_u^j + v_l^j) \\ v_{sum}^j \triangleq v_u^j + v_l^j \\ i_{sum}^j \triangleq \dfrac{1}{2}(i_u^j + i_l^j) \\ R \triangleq R_s + R_g + \dfrac{R_a}{2} \\ L \triangleq L_s + L_g + \dfrac{L_a}{2} \end{cases} , \quad \begin{cases} v_u^j = -v_{diff}^j + \dfrac{1}{2}v_{sum}^j \\ v_l^j = v_{diff}^j + \dfrac{1}{2}v_{sum}^j \\ i_u^j = \dfrac{1}{2}i_s^j + i_{sum}^j \\ i_l^j = -\dfrac{1}{2}i_s^j + i_{sum}^j \end{cases} \tag{3}$$

being

v_{diff}^j: differential voltage, which is approximately equal to the AC voltage at the point of connection (u^j).

i_{sum}^j: additive current, which circulates from the upper to the lower arm of leg j.

v_{sum}^j: additive voltage, which is approximately equal to the sum of the DC poles voltages.

Adding and subtracting (1) and (2), using the variables change from (3) leads to

$$\frac{1}{2}(V_u^{DC} - V_l^{DC}) + v_{diff}^j - v_g^j - v_n = Ri_s^j + L\frac{di_s^j}{dt} \tag{4}$$

$$v_{sum}^j - (V_u^{DC} + V_l^{DC}) = -2R_a i_{sum}^j - 2L_a\frac{di_{sum}^j}{dt} \tag{5}$$

Eqs. (4) and (5) ($j = a, b, c$) only contain a single derivative term (i_s^j and i_{sum}^j, respectively), therefore being suitable for state-space representation for small-signal analysis.

The voltage applied by the arms and the current flowing through them may contain AC and DC terms, with different roles in the power exchange and the energy stored in the converter. This is summarized in Table I and all the details can be found in [8].

As will be seen in the next section, the control of AC inner current magnitudes i_{sum}^{+-0} is not included in the linear model for simplicity. These components are relevant for DC pole imbalance studies, allowing for the energy balance between the upper and lower arms of each leg [21]. With this assumption, the system is SSTI and therefore suitable for linearization. Using the following definitions

$$V_{off}^{DC} \triangleq \frac{1}{2}(V_u^{DC} - V_l^{DC}) \ , \quad V_t^{DC} \triangleq V_u^{DC} + V_l^{DC} \tag{6}$$

combined with (4) and (5), yields

$$v_{diff}^{abc} - v_g^{abc} + (V_{off}^{DC} - v_n)(1\ 1\ 1)^T = R\boldsymbol{\mathcal{I}_3}i_s^{abc} + L\boldsymbol{\mathcal{I}_3}\frac{di_s^{abc}}{dt} \tag{7}$$

TABLE I

CONVERTER CURRENT COMPONENTS AND THEIR USES

Comp.	Freq.	Comp.	Use
i_s	AC	q,d	Current from the AC grid (Park coordinates).
		0	Equal to 0 due to three-wire connection.
	DC	α,β	Controlled to zero to prevent DC current flowing through the AC grid (Clarke coordinates).
		0	Equal to 0 due to three-wire connection.
i_{sum}	AC	+,-	Internal power exchange between upper and lower arms (Fortescue components).
		0	Controlled to zero to avoid AC distortion in the DC grid.
	DC	α,β	Internal power exchange between the legs of the converter (Clarke coordinates).
		0	Power flowing onto the DC grid.

$$v_{sum}^{\alpha\beta 0DC} - V_t^{DC}(0\ 0\ 1)^T = -2R_a\boldsymbol{\mathcal{I}_3}i_{sum}^{\alpha\beta 0DC} - 2L_a\boldsymbol{\mathcal{I}_3}\frac{di_{sum}^{\alpha\beta 0DC}}{dt} \tag{8}$$

$v_{diff}^{abc}, v_g^{abc}, i_s^{abc}, i_{sum}^{\alpha\beta 0DC} \in \mathbb{R}^3$ and being $\boldsymbol{\mathcal{I}_n} \in \mathbb{R}^{n\times n}$ the identity matrix. Note that Clarke transformation (see Appendix) is introduced for convenience [8].

Finally, an Average Arm Model (AAM) [22] has been considered for the six arms (see Fig. 2). Each equivalent capacitor voltage[1] $v_{Cul}^{abc} \in \mathbb{R}^6$ depends on the power exchanged by each arm, which is reflected as a charging current $i_{Cul}^{abc} \in \mathbb{R}^6$ in each capacitor circuit:

$$i_{Cul}^{abc} = C_{eq}\boldsymbol{\mathcal{I}_6}\frac{dv_{Cu}^{abc}}{dt} \tag{9}$$

B. MMC control

The overall control strategy, which has been shown conceptually in Fig. 3, is detailed in this section. Let MMC 1 be the master (DC voltage control) and let MMC 2 be the slave (active power control) (Fig. 1). The detailed control scheme for MMC 1 is shown in Fig. 4, which will be referred to as *classic control* from now on. All closed loops implemented use PI controllers, and different reference calculations are needed.

Referring to the top side, the DC voltage loop regulates the voltage at the DC side of terminal 1 (V_t^{DC}), yielding i_s^{q*} as output for the current loop. The other current reference (i_s^{d*}) is obtained through (10). Note that the AC side current control is implemented in a Synchronous Reference Frame (SRF) using Park transformation (see Appendix), obtaining v_{diff}^{qd} as output.

[1]Notation x_{ul}^{abc} will be used from now on, which is defined as: $x_{ul}^{abc} = (x_u^a\ x_u^b\ x_u^c\ x_l^a\ x_l^b\ x_l^c\ )^T$

$$i_s^{d*} = \frac{2}{3}\frac{Q_{ac}^*}{u^{q*}} \tag{10}$$

Regarding the bottom side, the energy loops control the total energy (W_t) and the energy difference between phases ($W_{a\to b}$ and $W_{a\to c}$). Also, a feed-forward structure using the AC power is added to the total energy controller. The total energy reference is set to the rated energy of the converter (11) and the energy difference references are set to zero. The total power, the power from phase a to phase b and the power from phase a to phase c references (energy controllers outputs) are defined as P_t^*, $P_{a\to b}^*$ and $P_{a\to c}^*$. Therefore, the additive DC current references in Clarke coordinates ($i_{sum}^{\alpha\beta 0DC^*}$) are calculated as (12).

$$W_t^* = 6\ \frac{1}{2}\frac{C_{SM}}{N_{arm}}\left(V_t^{DC^*}\right)^2 \tag{11}$$

$$\begin{bmatrix} i_{sum}^{\alpha DC^*} \\ i_{sum}^{\beta DC^*} \\ i_{sum}^{0DC^*} \end{bmatrix} = \frac{1}{3\ V_t^{DC^*}} \begin{bmatrix} 0 & 1 & 1 \\ 0 & \sqrt{3} & -\sqrt{3} \\ 1 & 0 & 0 \end{bmatrix} \begin{bmatrix} P_t^* \\ P_{a\to b}^* \\ P_{a\to c}^* \end{bmatrix} \tag{12}$$

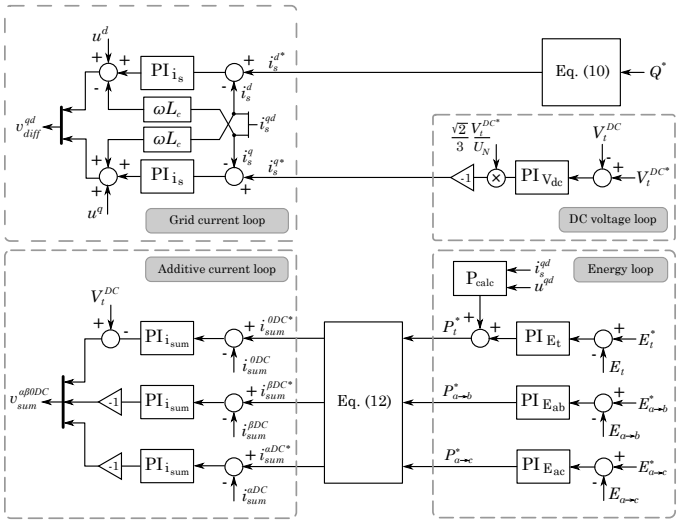

Fig. 4. Detailed MMC classic control scheme

Note that once the reference voltages v_{ul}^{abc} are calculated, the modulation indices m_{ul}^{abc} are calculated using the real capacitor voltages v_{Cul}^{abc} as

$$m_{ul}^{abc} = \frac{v_{ul}^{abc}}{v_{Cul}^{abc}} \tag{13}$$

C. HVDC cable modeling

Cable modeling has paramount importance in time-domain simulation. Lumped or distributed parameters models are the two most common approaches found in the literature. Regarding the first approach, simple or cascaded

π-sections are commonly used. With respect to the second approach, the wideband, also known as Universal Line Model (ULM), is usually the preferred alternative for accurate Electromagnetic Transient (EMT) simulations, as it is also frequency-dependent [23]. However, this kind of model cannot be translated directly into a state-space form. Recently, [24] addressed this issue, deriving a lumped parameters vector fitting based model with parallel branches that accurately reproduces the ULM behavior, being preferable to use a single parallel branches section rather than cascading several π-sections [24].

This model is shown in Fig. 5 (v^+ refers to the positive monopole, corresponding to $\frac{1}{2}V_t^{DC}$ in normal conditions). Recent studies have considered this model with a single section [13], [14]. In the present case, 5 sections have been considered in order to account for the hyperbolic correction factors, which improve the detail of the model specially for long cables. Furthermore, a wideband frequency-dependent cable model from the Best Paths project open source library [25] has been used in the time-domain simulations in order to show that the model is accurate. Taking $n \in \mathbb{N}$ as the number of sections, $1 + 4n$ differential equations are obtained (14). Note that (14d) is only necessary when $n \geq 2$

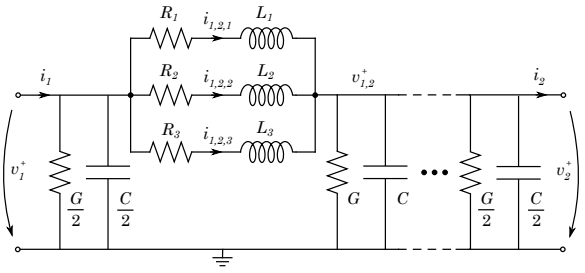

Fig. 5. Cable model with parallel series branches

$$\frac{dv_1}{dt} = \frac{4}{C}\left(i_1 - \sum_{k=1}^{3} i_{1,2,k} - \frac{G}{4}v_1\right) \tag{14a}$$

$$\frac{di_{i,i+1,k}}{dt} = \frac{1}{2L_k}v_1 - \frac{1}{2L_k}v_{i,i+1} - \frac{R_k}{L_k}i_{i,i+1,k},$$
$$i = 1, ..., n,\ k = 1, 2, 3 \tag{14b}$$

$$\frac{dv_2}{dt} = \frac{4}{C}\left(\sum_{k=1}^{3} i_{n,n+1,k} - i_2 - \frac{G}{4}v_2\right) \tag{14c}$$

$$\frac{dv_{i,i+1}}{dt} = \frac{2}{C}\left(\sum_{k=1}^{3} i_{i,i+1,k} - \sum_{k=1}^{3} i_{i+1,i+2,k} - \frac{G}{2}v_{i,i+1}\right),$$
$$i = 1, ..., n,\ n \geq 2 \tag{14d}$$

being

i_1, i_2: input and output currents of the cable.

v_1, v_2: total voltages at each cable terminal.

$v_{i,i+1}$: total voltage after section $i, i + 1$.

$i_{i,i+1,k}$: current flowing through section $i, i+1$, branch k.

R_k, L_k: equivalent pole resistance/inductance of branch k.

C, G: equivalent pole capacitance/admittance.

IV. System linearization

A linearized model of the system in state-space form is derived in order to analyze its small-signal characteristics. The complete state-space is represented by

$$\Delta\dot{x} = \mathbf{A}\Delta x + \mathbf{B}\Delta u \ , \quad \Delta y = \mathbf{C}\Delta x + \mathbf{D}\Delta u \tag{15}$$

being $\Delta x \in \mathbb{R}^{92}$ the state vector (including the states from MMC 1, MMC 2 and the cable), $\Delta u \in \mathbb{R}^{14}$ the inputs vector and $\Delta y \in \mathbb{R}^{30}$ the outputs vector (in this case, Δy contains some relevant states).

$$\begin{aligned} \Delta u &= (\Delta V_t^{DC^*}, \Delta P_2^*, \Delta E_{t,ab,ac,12}^*, \Delta i_{s,12}^{d^*}, \Delta v_{g,12}^{qd}) \\ \Delta y &= (\Delta i_{s,12}^{qd}, \Delta u_{12}^{qd}, \Delta i_{sum,12}^{\alpha\beta 0DC}, \Delta v_{ul-s,12}^{abc}, \Delta V_{12}, \Delta i_{12}) \end{aligned} \tag{16}$$

$\mathbf{A} \in \mathbb{R}^{92\times92}$, $\mathbf{B} \in \mathbb{R}^{92\times14}$, $\mathbf{C} \in \mathbb{R}^{30\times92}$ and $\mathbf{D} \in \mathbb{R}^{30\times14}$ are the state-space matrices, which have not been included here as they are too large. However, the system can be derived by observing the block diagram in Fig. 6 and using the equations shown in this section and the previous one.

A. MMC linearization

Both (7) and (8) are linear equations. However, due to the power balance needed in the AAM, (9) has to be linearized. This leads to:

$$\frac{d}{dt}\Delta v_{Cul}^{abc} = \frac{1}{C_{eq} v_{Cul0}^{abc}} \Delta P_{ul}^{abc} - \frac{P_{ul\ 0}^{abc}}{C_{eq} {v_{Cul0}^{abc}}^2} \Delta v_{Cul}^{abc} \tag{17}$$

being $\Delta v_{Cul}^{abc} \in \mathbb{R}^6$ the capacitors voltages and $\Delta P_{ul}^{abc} \in \mathbb{R}^6$ the total power through the arms. Subindex 0 indicates the value at the linearization point. The total power through the arms contains AC and DC components that can be calculated independently with the corresponding voltages and currents (3), taking into account that $diff$ variables are purely AC and sum variables are purely DC. For the AC component ($P_{ul}^{AC,j} \in \mathbb{R}^2$), each phase is assumed to exchange a third of the total power (18), whereas the DC component ($P_{ul}^{DC,j} \in \mathbb{R}^2$) is calculated as (19) ($j = a, b, c$).

$$\Delta P_{ul}^{AC,j} = \frac{1}{3}\left(\frac{3}{2}\sum_{k=q,d}\left(\frac{1}{2}\Delta v_{diff}^k i_{s\,0}^k + \frac{1}{2}\Delta i_s^k v_{diff\,0}^k\right)\right) \tag{18}$$

$$\Delta P_{ul}^{DC,j} = \frac{1}{2}\Delta v_{sum}^{0DC} i_{sum\,0}^{jDC} + \frac{1}{2}\Delta i_{sum}^{jDC} v_{sum\,0}^{jDC} \tag{19}$$

B. Control system linearization

Linearization of the PLL, arm energy calculation and AC power (the latter only needed in the slave) is required. The PLL tracks the angle of the voltage at the point of connection u. It is aligned with the component u^q by means of controlling u^d to 0 with a PI controller. The angle deviation effect introduced by the dyanamics of the PLL can be linearized as

$$\Delta e_\theta = -\frac{k_{p-pll}s + k_{i-pll}}{s^2 + u_0^q k_{p-pll}s + u_0^q k_{i-pll}}\Delta u^d \tag{20}$$

This angle is necessary for the transformation between the converter qd magnitudes (x^{qdc}), which are used in the control system framework, and the grid qd magnitudes (x^{qd}), which are obtained from the plant [26]. The transformations used can be found in the Appendix.

On the other hand, the energy of each arm ($W_{ul}^{abc} \in \mathbb{R}^6$) is linearized as (21) and the AC power as (22).

$$\Delta W_{ul}^{abc} = C_{eq} v_{Cul\,0}^{abc} \Delta v_{Cul}^{abc} \tag{21}$$

$$\Delta P = \frac{3}{2}\left(u_0^q \Delta i_s^q + \Delta u^q i_{s\,0}^q + u_0^d \Delta i_s^d + \Delta u^d i_{s\,0}^d\right) \tag{22}$$

C. Overall linearized system

The whole linear system is depicted in Fig. 6. The validation of the linearized model is performed through a time-domain simulation with Matlab® Simscape Power Systems™, comparing both the complete non-linear and the linearized models. A 10 % step change of the power injected from MMC 2 (ΔP_2) is applied. Parameters of the system can be found in Tables II and III (Appendix). The response of different magnitudes (MMC 1) is shown in Fig. 7.

V. Alternative control structures

The classic control scheme presented in Section III (Fig. 4) is widely reported in early work in literature and it is inspired on the common control schemes for 2-level VSC: the outer DC voltage loop yields the active current reference for the AC side current loop, and due to that fact the total energy loop has to yield the circulating current loop reference. This structure relies on the assumption that there is a relatively big capacitance in the DC side of the converter. Otherwise, notable transient deviations of the DC voltage are obtained when there is a change in the DC power flowing through the link. Whereas in a non-energy based control strategy a capacitance equal to $6 \cdot C_{SM}/N_{arm}$ can be included in the model according to [6], in the case of an energy-based approach the model does not contain such equivalent capacitance. Then, if the classic control scheme is used in a point-to-point HVDC link, some dynamics will depend strongly on the equivalent capacitance of the cable, i.e. the length of the line.

In the MMC, the power balance between the AC and the DC sides is not instantaneous as in the 2-level VSC case, as the MMC's arms act as an energy buffer. Therefore, it is intuitive to consider cascading the DC voltage loop with the DC current loop (which corresponds to three times i_{sum}^{0DC}) instead of the AC side current loop (i_s^q).

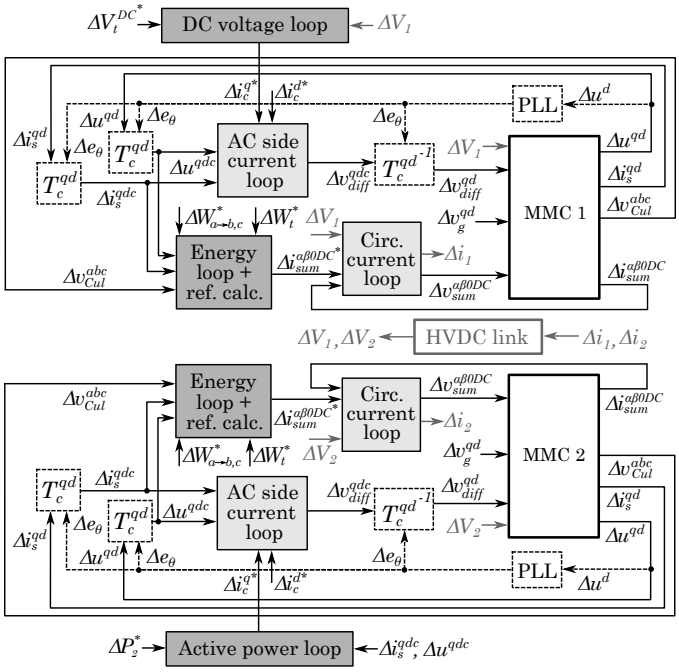

Fig. 6. Complete linear model of the system (classic control scheme)

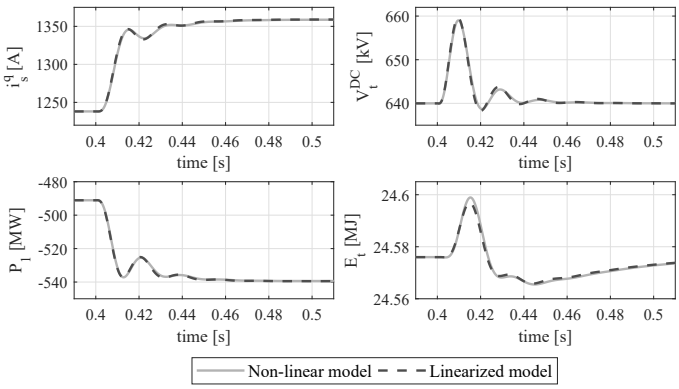

Fig. 7. Time-domain simulation comparison between the complete non-linear model and the linearized model (MMC 1)

This leads to a different control structure, shown in Fig. 8, and referred to as *cross control* from now on. Note that the control of the energy balance between phases remains unchanged.

With all above, a new control structure can be considered, consisting of the summation of the outer controllers outputs multiplied by weight factors k_1, k_2, k_3 and k_4 (Fig. 9). This option arises as a generalized structure, containing both the classic and the cross approaches as particular cases and a whole range of intermediate options. This structure will be referred to as *weighted control*. Parameters K_i ($i = 1...4$) from Fig. 9 are defined as follows (23), taking into account the corresponding unit conversion ratio preserving the same tuning for the DC voltage and energy controllers.

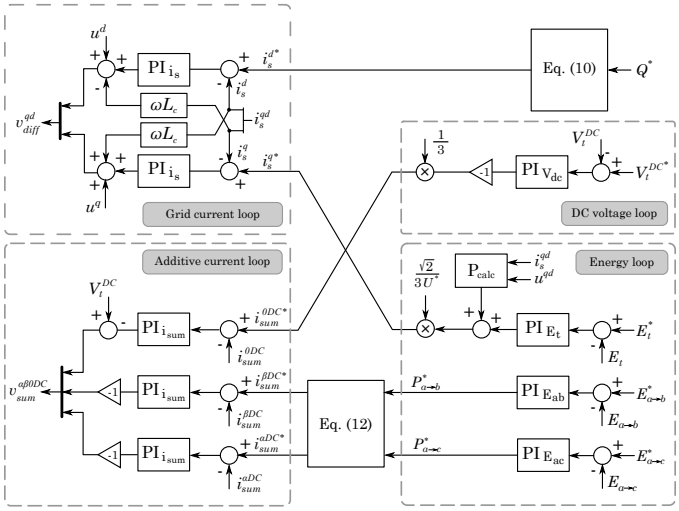

Fig. 8. Detailed MMC cross control scheme

$$K_1 = \frac{\sqrt{2}}{3}\frac{V_t^{DC*}}{U^*}k_1 \ , \ K_2 = -\frac{\sqrt{2}}{3}\frac{1}{U^*}k_2$$
$$K_3 = \frac{1}{3}k_3 \ , \ K_4 = \frac{1}{3}\frac{1}{V_t^{DC*}}k_4 \tag{23}$$

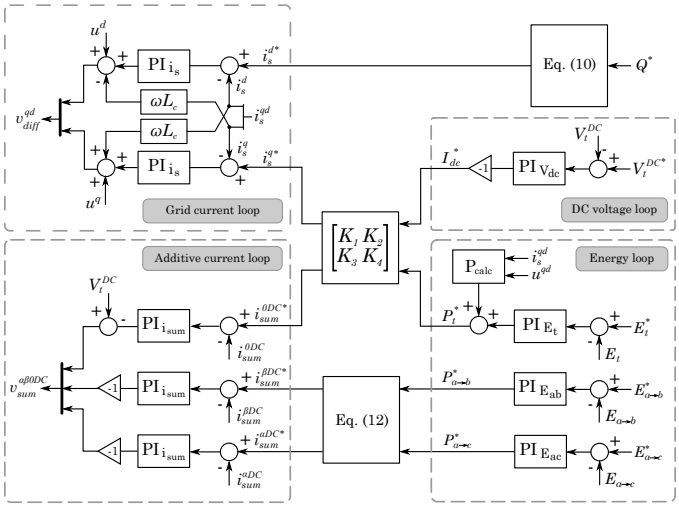

Fig. 9. Detailed MMC weighted control scheme

In the case of short and very short lines, however, the problem of the aforementioned approaches is that the capacitance at the DC terminals is very small, which may cause large voltage deviations during transients (this will be thoroughly analyzed in the next section). For this reason, a new control alternative should be explored. Such alternative consists of eliminating the DC side closed-loop in the cross control option, making it open-loop with a constant reference for v_{sum}^{0DC} which is the DC voltage set-point (V_t^{DC*}). The control scheme is shown in Fig. 10,

and it will be referred to as *constant DC voltage control*. This scheme would be also suitable for the back-to-back case, which is the most extreme case of a very short line.

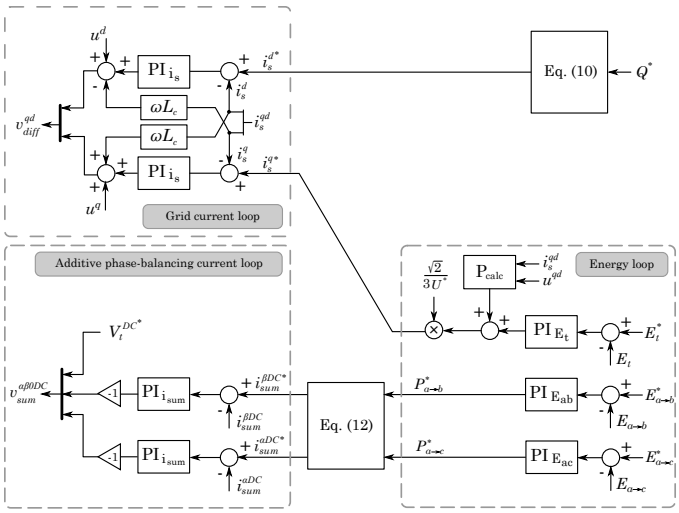

Fig. 10. Detailed MMC constant DC voltage control scheme

VI. Evaluation of the control performance and analysis of control structures

This section aims to show a qualitative comparison of the different control structures presented before, to shed some light on how to improve the transient behavior of the MMC.

In order to do a fair comparison of the performance for different cable lengths, a tuning criteria has to be established. On one hand, the current loops (i_s and i_{sum}^{DC}) are tuned to achieve a very fast response, according to the real modulation limits of the converter [20]. Such inner controllers are the physical limit of the converter control action or, in other words, the maximum speed response of the converter. Here, the current controllers have been designed to give a first-order closed-loop response with a time constant $\tau_{cc} = 1$ ms using Internal Model Control [27]. The PLL is tuned to track the grid angle within approximately 20 ms [28]. On the other hand, the energy controller has been designed considering a disturbance rejection problem and using a loop shaping strategy, specifying the maximum energy deviation and settling time [8]. The DC voltage controller (master converter) is designed considering the cable equivalent capacitance seen by the converter as the plant, deriving the closed-loop and specifying the settling time and the natural frequency of such a second order system. More specifically, these constants are calculated as

$$k_P = \frac{1}{2}\xi\omega_n C \ , \ k_I = \frac{1}{4}\omega_n^2 C \tag{24}$$

taking $\xi = 0.707$ and $\omega_n = 2\pi\dfrac{1}{15\tau_{cc}}$ to have enough time-scale separation between the current and the DC voltage controllers [27]. The AC power controller (slave converter) is designed using optimization robust control techniques, specifying a first order response of 100 ms [29], .

Regarding the transient performance, two possible extreme test case scenarios are identified:

- Case 1: an AC power reference change from 0 % to 100 % in the slave converter.
- Case 2: a sudden disconnection of the slave converter. Whereas it makes no sense to consider the previous case with an instantaneous power step change from 0 % to 100 %, it does make sense to consider the case of a faster change from 100 % to 0 %, in a possible contingency situation.

Although case 1 input signal is smoother than case 2, the latter allows for a bigger current transient: the power input changes from 1 pu to 0, an overshoot until -1 pu plus an admissible margin (within the converter limits) is acceptable. On the other hand, in case 1, as power changes from 0 to 1 pu, only an overshoot corresponding to the admissible margin is acceptable. Then, it is not clear whether a tuning that meets the transient requirements for case 1 will meet them for case 2. Therefore, an AC power response (slave converter) with a settling time of 40 ms is implemented. This is more restrictive than case 1 (100 ms) and allows to take into account a faster disconnection (case 2) and to highlight the transient differences between the control structures. The reason to choose 40 ms is that for the comparison shown, with lower values the transient response obtained would be very large, even obtaining negative voltages in the DC side.

The small-signal analysis will be performed under this assumption for the AC power loop, and the performance will be verified through the non-linear time-domain simulation model. For the frequency-domain analysis, the following transfer functions are of interest:

- $G_1(s)$: transfer function between $V_t^{DC}(s)$ and $P_2(s)$
- $G_2(s)$: transfer function between $E_t(s)$ and $P_2(s)$
- $G_3(s)$: transfer function between $i_s^{q*}(s)$ and $P_2(s)$
- $G_4(s)$: transfer function between $i_{sum}^{0DC*}(s)$ and $P_2(s)$

The specifications are defined imposing a limit in the maximum singular values (25) of such transfer functions:

$$\overline{\sigma}(G_i(0)) \leq \frac{\|y_i(0)\|_2}{\|u_i(0)\|_2} \tag{25}$$

being $u_i(0)$ the input and $y_i(0)$ the corresponding output:

- $u_i(0) = P_N$, $i = 1, 2, 3, 4$
- $y_1(0) = 0.10\ V_t^{DC*}$ (10% overvoltage)
- $y_2(0) = 0.10\ E_t^*$ (10% energy overshoot)
- $y_3(0) = 1.20\ (P_N/(3V_t^{DC*}))$ (20% i_{sum}^{0DC} overcurrent)
- $y_4(0) = 1.20\ (\sqrt{2}V_t^{DC*}/(3U_N))$ (20% i_s^q overcurrent)

With all above, time-domain and frequency-domain analyses are performed. Transient performance of MMC with the classic, cross, weighted and constant DC voltage control structures can be compared, for different cable lengths. The parameters of the system can be found in Tables II and III (Appendix), and all the controllers constants remain unchanged except for the DC voltage, which is tuned according to the cable length capacitance as mentioned before (24). For the time-domain simulations, a change from 0 to the rated power is performed at $t = 0.4$ s, and vice versa at $t = 0.65$ s.

In Figs. 11 and 12, classic and cross structure cases are shown. In the first place, a relevant difference between the smoothness of the dynamics is noticeable. It is worth noting that in the classic control structure dynamics are more coupled than in the cross control structure: a change in the DC side will directly affect i_s^{q*}, changing the AC side power, in turn affecting i_{sum}^{0DC*}. This effect is more remarkable as the length of the line decreases.

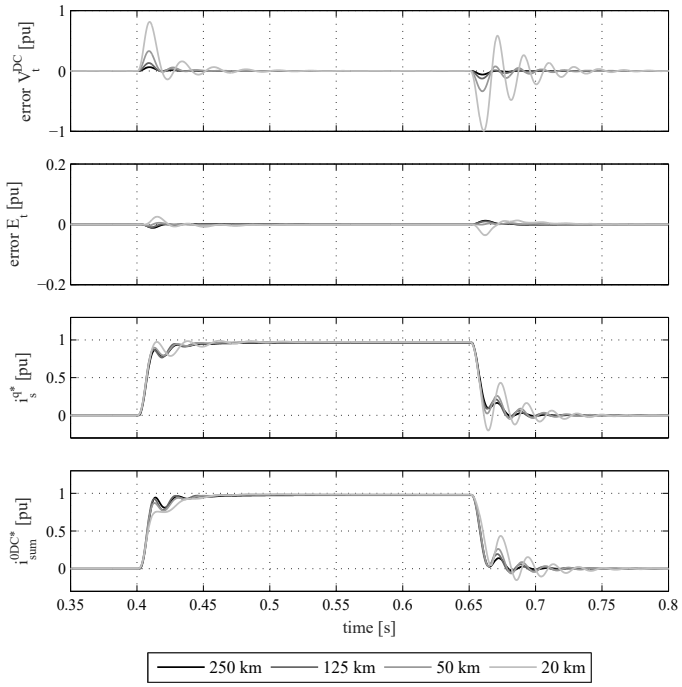

Fig. 11. Transient response of MMC 1 (classic control structure)

In the case of the cross control structure, dynamics of the DC side are clearly decoupled from the AC side. In other words, the energy loop will impose its slow dynamics in the AC side even though there is a sudden change of the power in the DC side. Also, the DC magnitudes are smoother. In conclusion, better performance is obtained in general, specially for shorter links. Nevertheless, the energy deviation appears to be larger than in the classic structure.

It has to be noted that very large deviations are obtained, specially in the DC voltage (in the classic alternative, almost double the voltage in the 20 km case in the first power change and almost zero voltage in the second power change). This of course would not be acceptable in reality, but it is shown as a way to highlight the problems that can be found with these alternatives in short lines cases.

Eigenvalue comparison from 3 km to 250 km is shown in Figs. 13 and 14. The oscillation modes and corresponding dampings are different for each alternative. This can be seen qualitatively with the imaginary part of the poles (which corresponds directly to the oscillation frequency of that particular mode, in rad/s) and with the angle formed by the vertical axis and and the segment between a particular pole and the origin (the smaller the angle, the smaller the damping). A quadratic scale has been used in order to show more cases of short lines.

Note that a complex unstable mode appears when the length of the line is decreased below a certain value. In

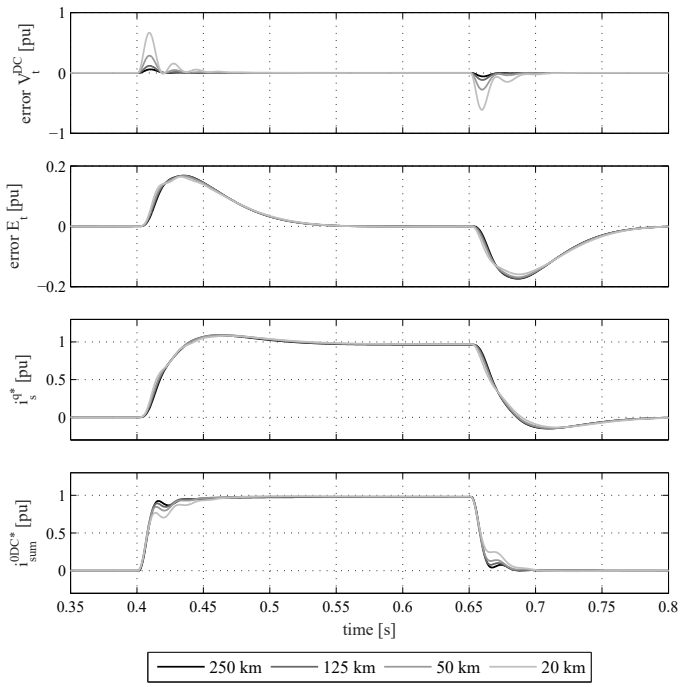

Fig. 12. Transient response MMC 1 (cross control structure)

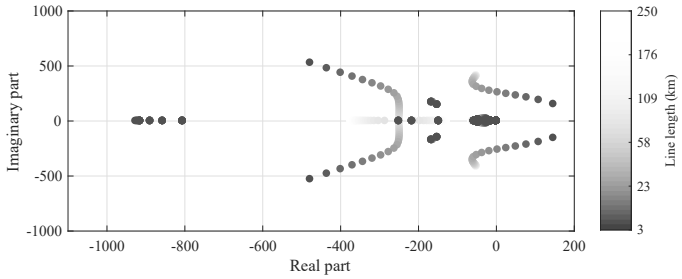

Fig. 13. Eigenvalue plot for different lengths of the line (classic control structure)

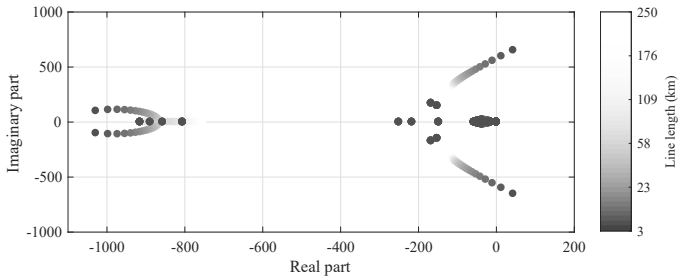

Fig. 14. Eigenvalue plot for different lengths of the line (cross control structure)

particular, with the control parameters used, for the classic structure (Fig. 13) this value is around 12 km, and for the cross structure (Fig. 14) it is around 5 km. Participation factors of such mode (namely $\lambda_{1,2}$) are shown in Figs. 15 and 16. Note that ζ indicates the integral state of a particular state variable, and subindex 1 or 2 refers to the master (MMC 1) or the slave (MMC 2), respectively.

Regarding the classic control case, the strongest contribution are the arm capacitor's voltages of both converters (specially MMC 1) and the cable. Also, it is remarkable the participation of the integral state of V_t^{DC} of MMC 1. This means that the tuning of both energy controllers has a remarkable effect on the eigenvalues of the system, as well as the DC voltage controller. Also, even though it is small compared to the others, there is a participation of the AC current, due to the structure of the classic control.

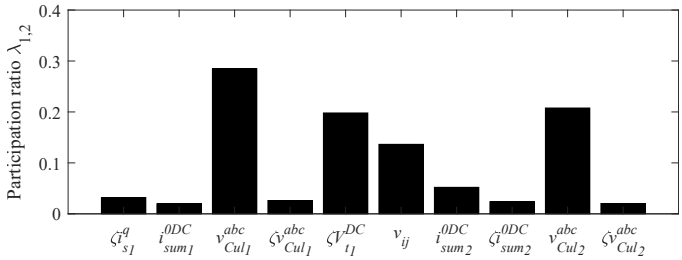

Fig. 15. Participation factors of the unstable mode $\lambda_{1,2}$ (classic control structure, line length of around 12 km)

With respect to the cross control, a strong participation of the cable is observed, too. In this case, the importance of the DC voltage control of MMC 1 is reduced. A major role is played by MMC 2, with the arm capacitor's voltages again. Furthermore, the DC current participates more than in the previous case, due to the fact that in the cross structure, the DC current control is directly connected to the DC voltage control. Here, the AC current does not play any role.

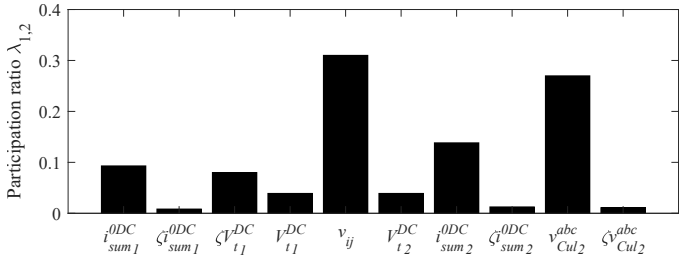

Fig. 16. Participation factors of the unstable mode $\lambda_{1,2}$ (cross control structure, line length of around 5 km)

The weighted alternative raises a new range of possibilities. Therefore, the transient response is evaluated for a parametric sweep between the classic ($k_1 = 1$, $k_2 = 0$, $k_3 = 0$ and $k_4 = 1$) and the cross ($k_1 = 0$, $k_2 = 1$, $k_3 = 1$ and $k_4 = 0$) options, for a 50 km line (Fig. 17). For this generic structure, intermediate results between both options are obtained. Weight factors have been changed proportionally between 0 and 1, or vice versa. Basically, it is shown that the cross structure performs better in all magnitudes during the transient, except for the energy

deviation, which is the highest. Then, an intermediate solution could make sense in order to achieve acceptable performance in all magnitudes.

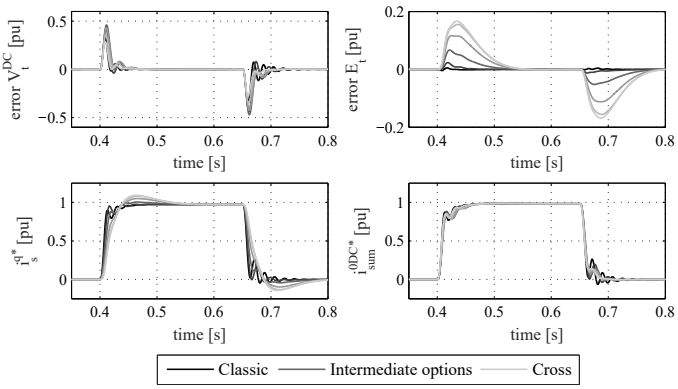

Fig. 17. Transient response of MMC 1, parametric sweep between classic and cross structures for a 50 km line (weighted control structure)

This alternative enables a whole range of combinations and would require a thorough tuning in order to clearly see its specific advantages in a particular case, as it has more degrees of freedom than the classic and cross structure cases (weight factors do not have to be only between 0 and 1, and they could be also negative). The purpose here is to show that a compromise solution could be taken. In order to compare this alternative with the others under the same conditions, the case of $k_1 = k_2 = k_3 = k_4 = 1$ has been chosen. Time-domain response and eigenvalue representation are shown in Figs. 18 and 19. Note that it is a combination of previous Figs. 13 and 14. Also, with these parameters, a slightly better performance is obtained compared to the cross control case (Fig. 12).

Regarding the constant DC voltage alternative, Fig. 20 shows the time-domain response for the same cases than before. The most remarkable thing is that the DC voltage error is tremendously small for the whole range of line lengths, compared to the previous cases. The reason is that the converter is generating a constant DC voltage without any dynamics behind it. The main concern, however, is that some oscillations appear, not only for the short line cases but also for the long line ones. This is observed specially in the DC voltage (Fig. 22). Also, note that the energy response is practically the same as in the cross option (Fig. 12), as these two alternatives decouple the AC and DC sides.

Regarding the eigenvalues (Fig. 21), it is worth noting that the system is still stable for very short lines, as the critical eigenvalue approaches the vertical axis asymptotically. However, the shorter the line the higher the frequency and the lower the damping of that mode.

In order to extend the transient results obtained to the whole frequency range, the singular values representation of all cases is shown in Fig. 23. In these plots it can be seen whether one particular case of a particular control structure exceeds or not the four transient requirements presented before, as a way to compare qualitatively different alternatives, maintaining the same tuning rules. Note that the peaks in the high frequency range are due to the distributed parameters cable model. However, this is not relevant as the attenuation is very high for those frequencies.

Results are consistent with the corresponding time-domain simulations. It is remarkable that in the classic alternative (Fig. 23a) there are peaks at different frequencies, whereas in the cross alternative (Fig. 23b) the peaks

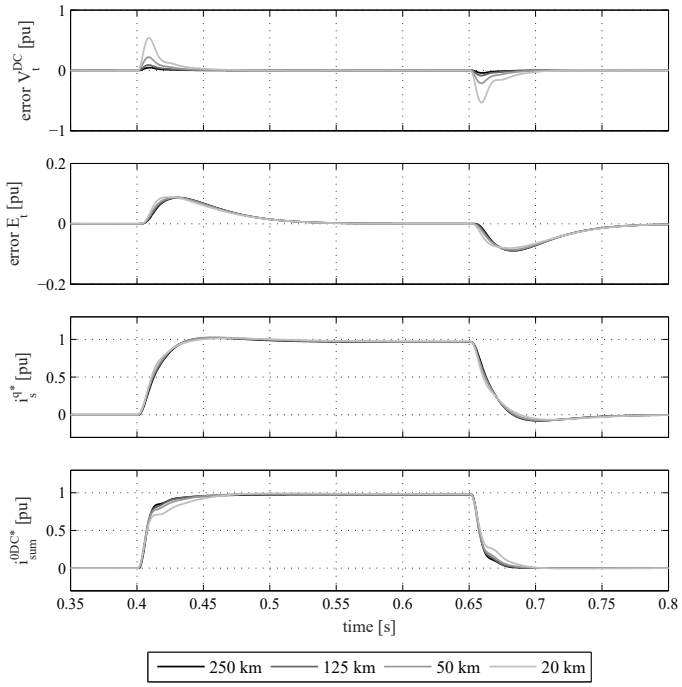

Fig. 18. Transient response of MMC 1 (weighted control structure, $k_1 = k_2 = k_3 = k_4 = 1$)

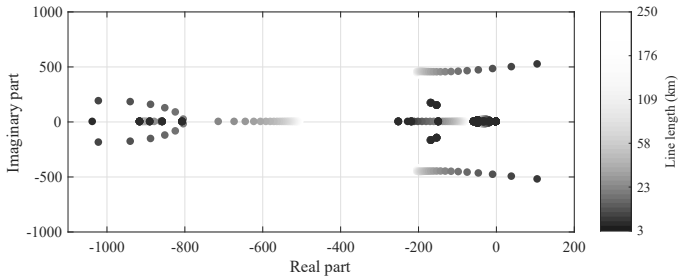

Fig. 19. Eigenvalue plot for different lengths of the line (weighted control structure, $k_1 = k_2 = k_3 = k_4 = 1$)

are reduced. This is shown also in the time-domain response (Figs. 11 and 12), which is smoother when using the second structure. Regarding the weighted case, it again proves that it is an intermediate option between the classic and the cross alternatives. As mentioned before, the case shown corresponds to $k_1 = k_2 = k_3 = k_4 = 1$. Again, a more thorough study should be conducted here analyzing different possibilities of the control system overall. Finally, the constant DC voltage structure presents the lowest error for the DC voltage. However, a steady-state error (left part of Fig. 23d, $G_1(s)$) is observed, even though it is very small. Also, resonant peaks are more noticeable than in other alternatives.

It has to be noted that most of the cases do not meet the constraints, specially the DC voltage, within a certain range of frequencies (see the curves exceeding the dashed line), which is consistent with the corresponding time-domain simulations (Figs. 11, 12, 18 and 20). This is because the transient requirements imposed (40 ms response for a rated power change) are rather strict. The purpose of the results shown here is not to find the best tuning

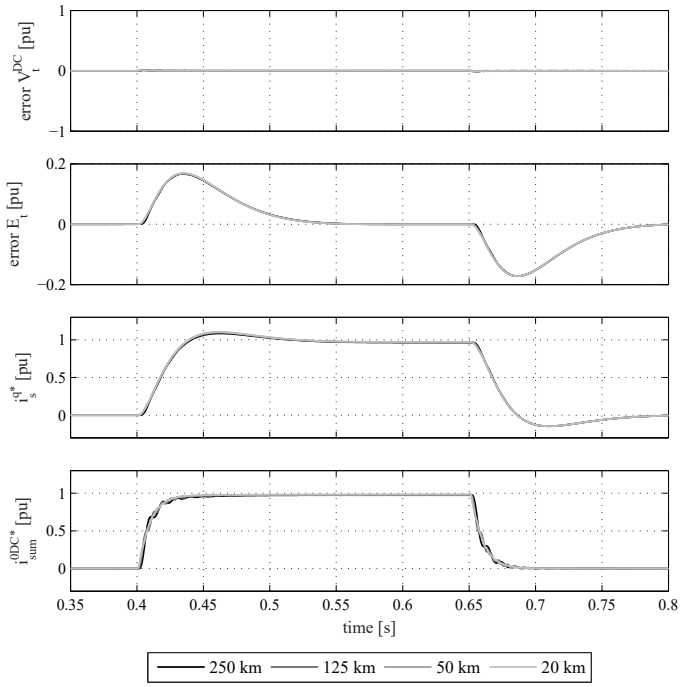

Fig. 20. Transient response of MMC 1 (constant DC voltage control structure)

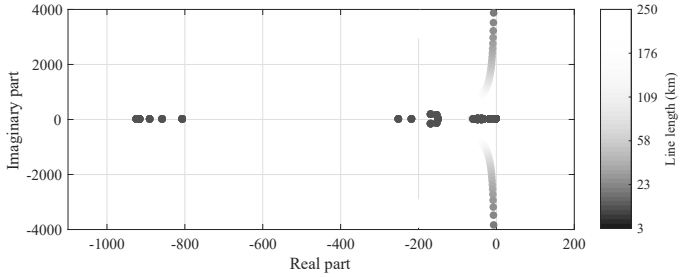

Fig. 21. Eigenvalue plot for different lengths of the line (constant DC voltage control structure)

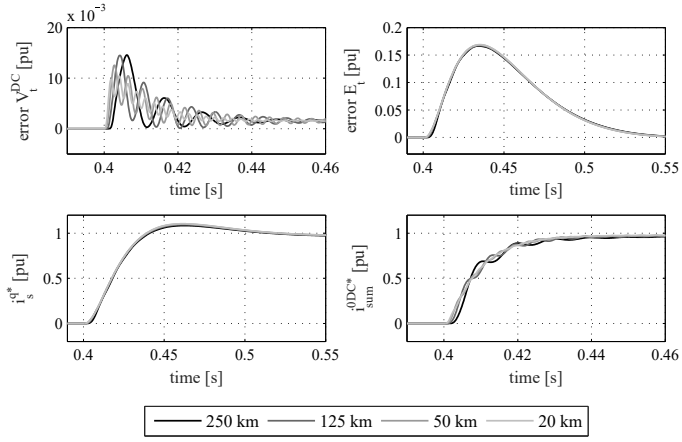

Fig. 22. High frequency oscillations (zoom of Fig. 20)

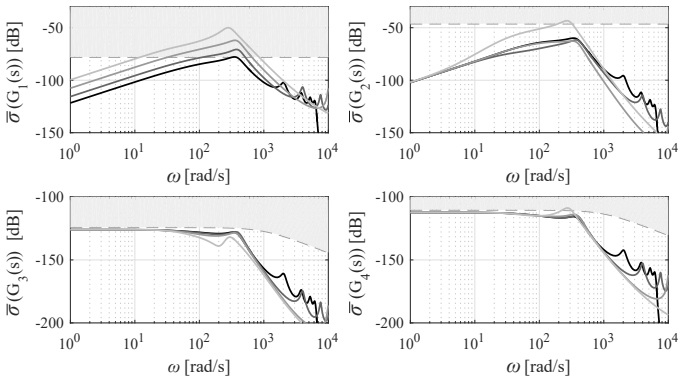

(a) Classic control structure

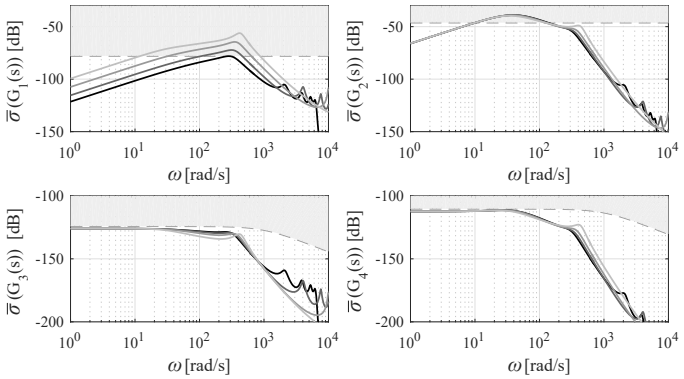

(b) Cross control structure

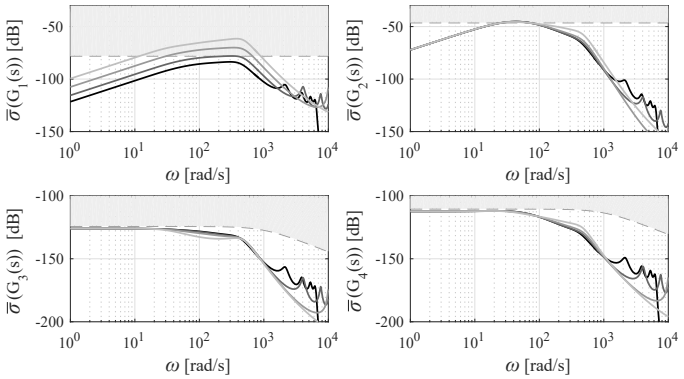

(c) Weighted control structure

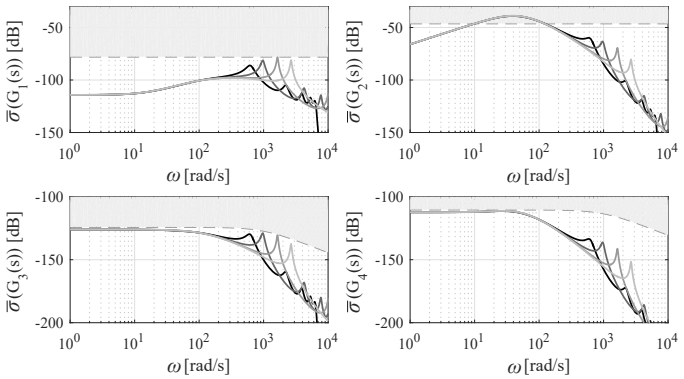

(d) Constant DC voltage control structure

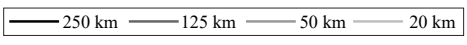

Fig. 23. Singular values representation of $G_i(s)$ $(i = 1...4)$ and gain limits

that meets the requirements, but to show a fair comparison between the different alternatives, highlighting the differences. Then, one alternative could be chosen more intuitively depending on the particular application, and a proper tuning that meets the requirements could be further investigated.

VII. Conclusion

Different alternatives for the control of a point-to-point MMC-HVDC link based on a master-slave strategy have been evaluated. A complete linear model of the system that enables linear analysis has been derived, complementing time-domain simulations with eigenvalue and frequency-domain analysis. Results show that the classic two-level VSC control structure extrapolated to the MMC (i.e. using the DC voltage control output as a reference for the AC active current, and therefore the total energy control output as a reference for the DC current) does not perform well for medium and short links, due to the high reduction of the capacitance in the DC bus, which depends exclusively on the cable length. A cross structure (i.e. using the DC voltage control output as a reference for the DC current, and the total energy control output as a reference for the AC active current) has demonstrated to improve the results, as the AC and the DC sides are notably decoupled. Also, a generic weighted structure combining both options has been presented, which enables a control system with more degrees of freedom that could be helpful to adjust the final transient response through a thorough tuning. However, for links of a few kilometers and back-to-back applications these alternatives may still lead to an unacceptable transient performance, or even instability. A constant DC voltage open-loop control has been evaluated as a possible solution, improving the DC voltage transient response and simplifying the control system, but showing some undesired oscillations and a small steady-state DC voltage error on the other hand.

Appendix

Transformations and parameters of the system

The following Clarke (26) and Park (27) transformations have been used. Note that regarding Park transformation, the electrical machinery notation ($qd0$) [30] is used.

$$\Theta^{\alpha\beta 0} \triangleq \frac{1}{3}\begin{bmatrix} 2 & -1 & -1 \\ 0 & -\sqrt{3} & \sqrt{3} \\ 1 & 1 & 1 \end{bmatrix} \Theta^{abc} \tag{26}$$

$$\Theta^{qd0} \triangleq \frac{2}{3}\begin{bmatrix} \cos(\theta) & \cos(\theta - \frac{2\pi}{3}) & \cos(\theta + \frac{2\pi}{3}) \\ \sin(\theta) & \sin(\theta - \frac{2\pi}{3}) & \sin(\theta + \frac{2\pi}{3}) \\ \frac{1}{2} & \frac{1}{2} & \frac{1}{2} \end{bmatrix} \Theta^{abc} \tag{27}$$

Transformation (28) is used to obtain the feedback measures i_s^{qdc} and u^{qdc}, whereas the inverse transformation (29) is used in v_{diff}^{qdc} to obtain v_{diff}^{qd} (refer to Fig. 6 for the overall linear control scheme).

$$\Delta x^{qdc} = \mathbf{T_c^{qd}}(\Delta x^{qd}, \Delta e_\theta)^T \tag{28}$$

$$\Delta x^{qd} = \mathbf{T_c^{qd}}^{-1}(\Delta x^{qdc}, \Delta e_\theta)^T \tag{29}$$

$$\mathbf{T_c^{qd}} = \begin{bmatrix} \cos(e_{\theta 0}) & -\sin(e_{\theta 0}) & -\sin(e_{\theta 0})x_0^q - \cos(e_{\theta 0})x_0^d \\ \sin(e_{\theta 0}) & \cos(e_{\theta 0}) & \cos(e_{\theta 0})x_0^q - \sin(e_{\theta 0})x_0^d \end{bmatrix} \tag{30}$$

TABLE II

MMC AND AC GRID PARAMETERS [8]

Parameter	**Symbol**	**Value**	**Units**
Rated (base) active power	P_N	500	MW
Rated (base) AC-side voltage	U_N	320	kV rms ph-ph
Rated (base) DC-side voltage	V_{DC}	$\pm$320	kV
Grid short-circuit ratio	SCR	10	-
Coupling impedance	R_s+jL_s	0.01+j0.2	pu
Arm reactor impedance	R_a+jL_a	0.01+j0.2	pu
Converter modules per arm	N_{arm}	400	-
Average module voltage	V_{SM}	1.6	kV
Sub-module capacitance	C_{SM}	8	mF

TABLE III

CABLE PARAMETERS [31]

Symbol	**Value**	**Units**	**Symbol**	**Value**	**Units**
r_1	0.1265	Ω/km	l_1	0.2644	mH/km
r_2	0.1504	Ω/km	l_2	7.2865	mH/km
r_3	0.0178	Ω/km	l_3	3.6198	mH/km
c	0.1616	μF/km	g	0.1015	μS/km

REFERENCES

[1] M. Barnes and A. Beddard, "Voltage source converter HVDC links - The state of the art and issues going forward," in *Energy Procedia*, vol. 24, 2012, pp. 108–122.

[2] M. P. Bahrman and B. K. Johnson, "The ABCs of HVDC transmission technologies," *IEEE Power Energy Mag.*, vol. 5, no. 2, pp. 32–44, 2007.

[3] R. Adapa, "High-Wire Act," *IEEE Power Energy Mag.*, pp. 18–29, 2012.

[4] A. Lesnicar and R. Marquardt, "An innovative modular multilevel converter topology suitable for a wide power range," *Conf. Proc. of IEEE Bologna PowerTech*, vol. 3, pp. 272–277, 2003.

[5] G. Bergna, J. A. Suul, and S. D'Arco, "State-space modelling of modular multilevel converters for constant variables in steady-state," *IEEE 17th Workshop on Control and Modeling for Power Electronics, COMPEL*, 2016.

[6] L. Harnefors, A. Antonopoulos, S. Norrga, L. Angquist, and H. P. Nee, "Dynamic analysis of modular multilevel converters," *IEEE Trans. Ind. Electron.*, vol. 60, no. 7, pp. 2526–2537, 2013.

[7] L. Angquist, A. Antonopoulos, D. Siemaszko, K. Ilves, M. Vasiladiotis, and H.-P. Nee, "Open-loop control of modular multilevel converters using estimation of stored energy," *IEEE Trans. Ind. Appl.*, vol. 47, no. 6, pp. 2516–2524, 2011.

[8] E. Prieto-Araujo, A. Junyent-Ferré, C. Collados-Rodríguez, G. Clariana-Colet, and O. Gomis-Bellmunt, "Control design of Modular Multilevel Converters in normal and AC fault conditions for HVDC grids," *Electr. Power Syst. Res.*, vol. 152, pp. 424–437, 2017.

[9] Q. Tu, Z. Xu, and L. Xu, "Reduced Switching-frequency modulation and circulating current suppression for modular multilevel converters," *IEEE Trans. Power Del.*, vol. 26, no. 3, pp. 2009–2017, 2011.

[10] A. Antonopoulos, L. Angquist, and H.-P. Nee, "On dynamics and voltage control of the Modular Multilevel Converter," *13th European Conf. on Power Electronics and Applications, EPE-ECCE*, 2009.

[11] K. Sharifabadi, L. Harnefors, H. P. Nee, S. Norrga, and R. Teodorescu, *Design, control and application of modular multilevel converters for HVDC transmission systems*. John Wiley & Sons, 2016.

[12] A. J. Far and D. Jovcic, "Small-Signal Dynamic DQ Model of Modular Multilevel Converter for System Studies," *IEEE Trans. Power Del.*, vol. 31, no. 1, pp. 191–199, 2016.

[13] J. Freytes, S. Akkari, J. Dai, F. Gruson, P. Rault, and X. Guillaud, "Small-signal state-space modeling of an HVDC link with modular multilevel converters," *IEEE 17th Workshop on Control and Modeling for Power Electronics, COMPEL*, 2016.

[14] S. Akkari, E. Prieto-Araujo, J. Dai, O. Gomis-Bellmunt, and X. Guillaud, "Impact of the DC cable models on the SVD analysis of a Multi-Terminal HVDC system," *19th Power Syst. Computation Conf., PSCC*, 2016.

[15] E. Sánchez-Sánchez, E. Prieto-Araujo, and O. Gomis-Bellmunt, "Multi-terminal HVDC voltage droop control design considering DC Grid, AC Grid and MMC dynamics," in *13th IET Int. Conf. on AC and DC Power Transmission*, 2017.

[16] J. Freytes, G. Bergna, J. A. Suul, S. D'Arco, F. Gruson, F. Colas, H. Saad, and X. Guillaud, "Improving Small-Signal Stability of an MMC with CCSC by Control of the Internally Stored Energy," *IEEE Trans. Power Del.*, 2018.

[17] G. Bergna-Diaz, J. A. Suul, and S. D'Arco, "Small-signal state-space modeling of modular multilevel converters for system stability analysis," *Proc. of IEEE Energy Conversion Congr. and Exposition, ECCE*, pp. 5822–5829, 2015.

[18] J. Beerten, G. B. Diaz, S. D'Arco, and J. A. Suul, "Comparison of small-signal dynamics in MMC and two-level VSC HVDC transmission schemes," *IEEE Int. Energy Conf., ENERGYCON*, 2016.

[19] G. Bergna, J. A. Suul, and S. D'Arco, "Impact on small-signal dynamics of using circulating currents instead of AC-currents to control the DC voltage in MMC HVDC terminals," *Proc. of IEEE Energy Conversion Congr. and Expo., ECCE*, 2017.

[20] S. Debnath, J. Qin, B. Bahrani, M. Saeedifard, and P. Barbosa, "Operation, Control, and Applications of the Modular Multilevel Converter: A Review," *IEEE Trans. Power Electron.*, vol. PP, no. 99, pp. 1–1, 2014.

[21] A. Junyent-Ferre, P. Clemow, M. M. C. Merlin, and T. C. Green, "Operation of HVDC modular multilevel converters under DC pole imbalances," *16th European Conf. on Power Electronics and Applications, EPE-ECCE*, 2014.

[22] H. Saad, S. Dennetiere, J. Mahseredjian, P. Delarue, X. Guillaud, J. Peralta, and S. Nguefeu, "Modular multilevel converter models for electromagnetic transients," *IEEE Trans. Power Del.*, vol. 29, no. 3, pp. 1481–1489, 2014.

[23] A. Morched, B. Gustavsen, and M. Tartibi, "A universal model for accurate calculation of electromagnetic transients on overhead lines and underground cables," *IEEE Trans. Power Del.*, vol. 14, no. 3, pp. 1032–1038, 1999.

[24] J. Beerten, S. D'Arco, and J. A. Suul, "Frequency-dependent cable modelling for small-signal stability analysis of VSC-HVDC systems," *IET Gener. Transm. Distrib.*, vol. 10, no. 6, pp. 1370–1381, 2016.

[25] C. Ugalde-Loo *et al.*, "Open access simulation toolbox for the grid connection of offshore wind farms using multi-terminal HVDC networks," *13th IET Int. Conf. on AC and DC Power Transmission*, pp. 1–6, 2017.

[26] L. Zhang, "Modeling and Control of VSC-HVDC Links Connected to Weak AC Systems," Ph.D. dissertation, Royal Institute of Technology, 2010.

[27] A. Egea-Alvarez, A. Junyent-Ferré, and O. Gomis-Bellmunt, "Active and Reactive Power Control of Grid Connected Distributed Generation Systems," in *Modeling and Control of Sustainable Power Systems*. Springer, 2012, pp. 47–81.

[28] S. K. Chung, "A phase tracking system for three phase utility interface inverters," *IEEE Trans. Power Electron.*, vol. 15, no. 3, pp. 431–438, 2000.

[29] H. Saad, Y. Fillion, S. Deschanvres, Y. Vernay, and S. Dennetiere, "On Resonances and Harmonics in HVDC-MMC Station Connected to AC grid," *IEEE Trans. Power Del.*, vol. 32, no. 3, pp. 1565–1573, 2017.

[30] P. C. Krause, O. Wasynczuk, and S. D. Sudhoff, *Analysis of Electric Machinery and Drive Systems*. IEEE series on Power Eng., 2002.

[31] J. Freytes, "Small-signal stability analysis of Modular Multilevel Converters and application to MMC-based Multi-Terminal DC grids," Ph.D. dissertation, École centrale de Lille, 2017.

Enric Sánchez-Sánchez (S'15) received the degree in Industrial Engineering from the School of Industrial Engineering of Barcelona (ETSEIB), Technical University of Catalonia (UPC), Barcelona, Spain, in 2014. Since 2012, he has been with CITCEA-UPC, first as Intern and then as Project Engineer. Currently, he is pursuing the Ph.D. degree in Electrical Engineering at the UPC. His research interests include modeling, control and interaction of power electronics in the power system, HVDC networks and integration of renewable energy.

Eduardo Prieto-Araujo (S'12-M'16) received the degree in Industrial Engineering from the School of Industrial Engineering of Barcelona (ETSEIB), Technical University of Catalonia (UPC), Barcelona, Spain, in 2011, and the Ph.D. degree in Electrical Engineering from the UPC in 2016. Since 2010, he has been with the Centre dInnovació Tecnològica en Convertidors Estàtics i Accionaments (CITCEA-UPC). His research interests include the modeling and control of electrical machines, renewable energy integration in power systems and control of power electronic converters for HVDC transmission.

Adrià Junyent-Ferré (S'09-M'11) received the degree in Industrial Engineering from the School of Industrial Engineering of Barcelona (ETSEIB), Technical University of Catalonia (UPC) in 2007, and the Ph.D. degree in Electrical Engineering from the UPC in 2011. He was a Researcher at CITCEA-UPC from 2006 to 2012, and a Lecturer at the Barcelona College of Industrial Engineering (EUETIB) in 2012. He joined the Department of Electrical and Electronic Engineering at Imperial College London as a Research Associate in 2013 and became a Lecturer in September 2014. His research focuses on control of power electronic converters and their design, with specific focus on wind power, VSC-HVDC and microgrids.

Oriol Gomis-Bellmunt (S'05-M'07-SM'12) received the degree in Industrial Engineering from the School of Industrial Engineering of Barcelona (ETSEIB), Technical University of Catalonia (UPC), Barcelona, Spain, in 2001 and the Ph.D. degree in Electrical Engineering from the UPC in 2007. In 1999, he joined Engitrol S.L. where he worked as Project Engineer in the automation and control industry. Since 2004, he has been with the Electrical Engineering Department of the UPC where he is Professor and participates in the CITCEA-UPC Research Group. His research interests include the fields linked with electrical machines, power electronics and renewable energy integration in power systems.